https://doi.org/10.1016/j.geomorph.2017.12.005

# Accepted Manuscript

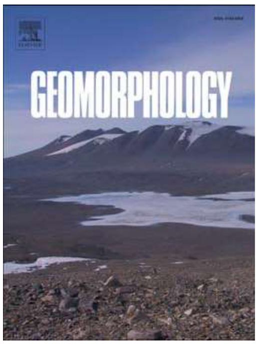

Extraction of multi-scale landslide morphological features based on local $G_i$* using airborne LiDAR-derived DEM

Wenzhong Shi, Susu Deng, Wenbing Xu

PII: S0169-555X(16)30435-4
DOI: doi:10.1016/j.geomorph.2017.12.005
Reference: GEOMOR 6246

To appear in: *Geomorphology*

Received date: 3 June 2016
Revised date: 6 November 2017
Accepted date: 3 December 2017

Please cite this article as: Shi, Wenzhong, Deng, Susu, Xu, Wenbing, Extraction of multi-scale landslide morphological features based on local $G_i$* using airborne LiDAR-derived DEM, *Geomorphology* (2017), doi:10.1016/j.geomorph.2017.12.005

# Extraction of multi-scale landslide morphological features based on local $G_i$* using Airborne LiDAR-derived DEM

Wenzhong Shi [a], Susu Deng [a, b,1], Wenbing Xu [b]

[a] *Department of Land Surveying and Geoinformatics, the Hong Kong Polytechnic University, Hong Kong – (john.wz.shi@polyu.edu.hk; augustran@163.com)*

[b] *School of Environment and Resource, Zhejiang Agriculture and Forestry University, Hangzhou, 311300, PR China – (augustran@163.com; xuwb@zafu.edu.cn)*

**Corresponding author**: Susu Deng. Tel: +0086 571 63711642. Email: augustran@163.com

---

[1] Present address: *School of Environment and Resource, Zhejiang Agriculture and Forestry University, Hangzhou, 311300, PR China*

# Extraction of multi-scale landslide morphological features based on local $G_i$* using Airborne LiDAR-derived DEM

## Abstract

For automatic landslide detection, landslide morphological features should be quantitatively expressed and extracted. High-resolution Digital Elevation Models (DEMs) derived from airborne Light Detection and Ranging (LiDAR) data allow fine-scale morphological features to be extracted, but noise in DEMs influences morphological feature extraction, and the multi-scale nature of landslide features should be considered. This paper proposes a method to extract landslide morphological features characterized by homogeneous spatial patterns. Both profile and tangential curvature are utilized to quantify land surface morphology, and a local $G_i$* statistic is calculated for each cell to identify significant patterns of clustering of similar morphometric values. The method was tested on both synthetic surfaces simulating natural terrain and airborne LiDAR data acquired over an area dominated by shallow debris slides and flows. The test results of the synthetic data indicate that the concave and convex morphologies of the simulated terrain features at different scales and distinctness could be recognized using the proposed method, even when random noise was added to the synthetic data. In the test area, cells with large local $G_i$* values were extracted at a specified significance level from the profile and the tangential curvature image generated from the LiDAR-derived 1-m DEM. The morphologies of landslide main scarps, source areas and trails were clearly indicated, and the morphological features were represented by clusters of extracted cells. A comparison with the morphological feature extraction method based on curvature thresholds proved the proposed method's robustness to DEM noise. When verified against a landslide inventory, the morphological features of almost all recent (< 5 years) landslides and approximately 35% of historical (> 10 years) landslides were extracted. This finding indicates that the proposed method can facilitate landslide detection, although the cell clusters extracted from curvature images should be filtered using a filtering strategy based on supplementary information provided by expert knowledge or other data sources.

**Keywords**: LiDAR; morphological feature extraction; local spatial pattern; landslide

## 1. Introduction

As a geologic process that occurs over a wide variety of spatial and temporal scales in mountainous areas, landslides leave discernible morphological features on topographic surfaces (Soeters and van Westen 1996). Through recognizing these morphological features, landslides can be detected and mapped to generate landslide inventory maps for further analysis of the landslide susceptibility of a given area and evolution of landscape affected by slope failures (Mackey and Roering 2011; Petschko et al. 2016). A variety of remote sensing techniques can be used to identify landslide morphological features (Ardizzone et al. 2007; Joyce et al. 2014), amongst which airborne Light Detection and Ranging (LiDAR) is popular due to its ability to provide high-quality, high-resolution Digital Elevation Models (DEMs) and to penetrate dense vegetation (Jaboyedoff et al. 2012; Guzzetti et al. 2012). LiDAR-derived DEMs allow fine-scale landslide morphological features to be recognized (McKean and Roering 2004; Glenn et al. 2006), even beneath dense vegetation.

For the purpose of automatic landslide detection and mapping, landslide morphological features should be quantitatively expressed and extracted. This is usually implemented using first- and second-order derivatives of elevation, e.g., slope, aspect, profile and tangential curvature. Tarolli et al. (2012) extracted landslide main scarps using both a curvature threshold determined based on Q-Q plots and slope values. However, calculating curvature is strongly scale-dependent, and the determination of curvature threshold is difficult in rough terrain. A few studies have utilized measures of topographical variability and surface roughness to extract landslide morphological features (Berti et al. 2013). Booth et al. (2009) applied two-dimensional Fourier and wavelet transforms to quantify and automatically map deep-seated landslide morphological features. Kasai et al. (2009) characterized the surface textures of deep-seated landslides using eigenvalue ratio and slope filters in order to extract potential sites of recent landslides. Those methods were proposed for large, deep-seated landslides that were characterized by relatively high topographical variability. However, landslide morphological features may have other topographic expressions, e.g., concave or convex morphologies, depending on the types, sizes and evolution stage of landslides (Soeters and van Westen 1996; Ardizzone *et al*. 2007). Therefore, methods should be developed to quantify and extract landslide morphological features characterized by various topographic expressions apart from the topographical variability of a specific pattern.

An important issue relevant to landslide morphological feature extraction using airborne LiDAR is scale. It is known that spatial phenomena are influenced by scale

(Turner et al. 1989). The size of landslides and hence the scale of landslide morphological features may vary greatly within the same area. Methods capable of extracting multi-scale morphological features are necessary. Kalbermatten et al. (2012) proposed a wavelet coefficient filtering procedure to analyze the multi-scale topographic variability of seven zones delimitated within a large landslide. Van Den Eeckhaut et al. (2012) and Li et al. (2015) exploited multi-resolution segmentation and supervised classification to extract landslide bodies. Although they considered the multi-scale characteristics of landslide morphological features, the selection of appropriate scales for segmentation has been a challenge, especially for landslides with complex morphologies. In addition, when extracting landslide morphological features, the noise contained in LiDAR-derived DEMs has much greater influence on small-scale features than on large-scale features (Passalacqua et al. 2010a; Li et al. 2011). It is more difficult to extract small-scale landslide morphological features under the effects of DEM noise. Therefore, methods for extracting multi-scale landslide morphological features should be robust to DEM noise.

In this study, a method based on the local $G_i$* statistic is proposed to quantify and extract landslide morphological features represented by concave or convex morphologies. The local $G_i$* statistic was introduced in Getis and Ord (1992) for the study of local patterns in spatial data. It is used in the proposed method to identify homogeneous patterns of clustering of similar morphometric values, i.e., concave or convex morphologies. The proposed method was first tested on synthetic surfaces to illustrate its capability to identify concave and convex morphologies and its robustness to DEM noise. The data from an airborne LiDAR survey flown over a test site in Hong Kong, within which shallow (<3 m depth of failure) debris slides and flows are abundant, was then utilized to test the proposed method for landslide morphological feature extraction. For comparison with the method proposed in this study, we also attempted to extract landslide morphological features represented by concave or convex morphologies solely based on curvature thresholds to assess the effects of DEM noise on the extraction results. Finally, the potential for using the proposed morphological feature extraction method to detect and map debris slides or flows was evaluated.

## 2. Methodology

### 2.1. Local $G_i$* statistic

Let $\{z_1, z_2, \ldots, z_n\}$ be a set of observations of a random variable acquired at different locations $(x_i, y_i)$ $(I = 1, 2, \ldots, n)$ over space. Local $G_i$*, as an indicator of local spatial association among observation values around the spatial location $i$, is defined by (Ord and Getis 1995)

$$G_i^* = \frac{\sum_{j=1}^{n} \mathbf{W}_{ij} z_j - \mathbf{W}_i^* \bar{z}}{s\left\{\left[(nS_{1i}^*) - \mathbf{W}_i^{*2}\right] / (n-1)\right\}^{1/2}}, \tag{1}$$

where **W** represents an $n$-by-$n$ matrix with

$$\mathbf{W}_i^* = \sum_{j=1}^{n} \mathbf{W}_{ij} \quad \text{and} \quad S_{1i}^* = \sum_{j=1}^{n} \mathbf{W}_{ij}^2 .$$

$\bar{z}$ and $s$ are the mean and the standard deviation of all observations, respectively.

The matrix **W** is a spatial weight matrix that defines spatial links among observations. A few schemes have been created to formulate spatial weight matrices, e.g., spatial contiguous neighbours, inverse distances, lengths of shared borders divided by the perimeter, and Gaussian distance decline (Getis and Aldstadt, 2004). A common way to construct the W matrix for the local statistic is to assign a weight of one to the observations within a pre-defined neighbourhood of each target location, and a weight of zero to those outside (Boots 2002; Nelson et al. 2007; Chu et al. 2009; Lanorte et al. 2013). In that case, the spatial weight matrix can be constructed using a distance threshold:

$$\mathbf{W}_{ij} = \begin{cases} 1 & \text{if } d_{ij} < D \\ 0 & \text{else} \end{cases} \quad i, j = 1, \ldots, n, \tag{2}$$

where $d_{ij}$ represents the distance between target spatial location $i$ and neighbouring location $j$, and $D$ is the specified distance threshold. A large distance threshold results in a large neighbourhood size. The size of the neighbourhood determines the scale of the spatial pattern to be recognized. Multi-scale spatial patterns can be revealed by local $G_i^*$ by changing the size of the neighbourhood (*e.g.*, Wulder and Boots 1998; Derksen et al. 1998; Nelson et al. 2007).

A large positive local $G_i^*$ value indicates clustering of high (i.e., large positive) observation values, whereas a large negative $G_i^*$ indicates clustering of low (i.e., large negative) observation values. Therefore, local $G_i^*$ can be utilized to identify the spatial pattern characterized by the clustering of very high or very low observation values. The distinctness of a local spatial pattern is measured through a statistical significance test. If the neighbourhood size is not smaller than 8 observations, the resulting distribution of local $G_i^*$ is normal (Griffith et al. 1996). The statistic given by Eq. (1) is in Z score standardized form. Consequently, the local $G_i^*$ values computed using Eq. (1) are directly compared with the critical value under a specified significance level to indicate the significance. If the absolute value of the local $G_i$* exceeds the critical value, the local spatial pattern is statistically significant.

## 2.2. Quantification of concave and convex morphology

To extract landslide features characterized by concave or convex morphologies, two terrain parameters, profile curvature and tangential curvature, are employed to quantify land surface morphology. Curvature is associated with the second derivatives of elevation and can be defined in various ways (Schmidt et al. 2003). Profile curvature and tangential curvature measure land surface shape in two different directions. Profile curvature measures the rate of change of slope gradient in the slope direction, i.e., the direction of the maximum slope (Schmidt et al. 2003). It affects flow acceleration and deceleration (Zevenbergen and Thorne 1987) and helps identify breaks in slope (Grohmann et al. 2011). It is defined as (Evans, 1972)

$$\kappa_{pr} = -\frac{f_{xx}f_x^2 + 2f_{xy}f_xf_y + f_{yy}f_y^2}{pq^{3/2}}, \text{ where } p = f_x^2 + f_y^2, \text{ and } q = 1 + p. \tag{3}$$

$f_x$ and $f_y$ are first-order partial derivatives, and $f_{xx}$, $f_{yy}$, and $f_{xy}$ are second-order partial derivatives. A positive (negative) profile curvature indicates the surface is convex (concave) in the slope direction.

Tangential curvature, which is defined in the direction normal to the slope direction, influences flow convergence and divergence (Zevenbergen and Thorne, 1987). It is formulated as (Krcho, 1991)

$$\kappa_{\tan} = -\frac{f_{xx}f_y^2 - 2f_{xy}f_xf_y + f_{yy}f_x^2}{pq^{1/2}}, \text{ where } p = f_x^2 + f_y^2, \text{ and } q = 1 + p, \tag{4}$$

using the same notation as for Eq. (3). A positive (negative) tangential curvature indicates the surface is convex (concave) in the direction perpendicular to the slope direction.

## 2.3. Morphological feature extraction method

The primary aim of this study is to extract landslide features characterized by concave or convex morphologies. Concave and convex morphologies can be expressed by clusters of similar negative and positive curvature values, respectively. Extracting landslide features characterized by concave or convex morphologies is hence regarded as the identification of the spatial pattern of clustering of similar negative or positive curvature values. The flowchart in Fig. 1 shows how to extract morphological features related to a specific scale. Both profile and tangential curvature are utilized to quantify land surface morphology along different directions. First, profile or tangential curvature is calculated on each DEM cell using Eqs. (3) or (4). The weight matrix is then constructed based on a predefined distance threshold. A single row in the matrix corresponds to a DEM cell, with matrix values of one designating the cells in its neighbourhood. The distance threshold determines the scale of the morphological features to be extracted. Subsequently, local $G_i$* is calculated cell by cell. The $G_i$* value on each cell indicates whether high or low curvature values cluster around the target cell. A significant local pattern of clustering of high or low curvature values can be revealed through the statistical significance test introduced in section 2.1. Finally, all cells with significant local spatial patterns are extracted to represent the target morphological features. According to the definition of curvature in section 2.2, a pattern of clustering of high curvature values indicates a convex morphology, whereas clustering of low curvature values indicates a concave morphology.

The procedures shown in Fig. 1 only allow for extracting morphological features related to a specific scale, but in most cases, the target morphological features are related to a series of scales. To extract morphological features related to multiple scales, the approach in Derksen et al. (1998) is employed. On each cell, local $G_i^*$ is calculated using different distance thresholds $D_1$, $D_2$, …, $D_k$. The largest positive or negative $G_i^*$ value for all distances is recorded on each cell for further analysis because it represents the maximization of the significance of the local spatial pattern around the centre cell (Derksen et al. 1998; Wulder and Boots 1998). The distance threshold series should be chosen based on the sizes of target morphological features and the DEM resolution.

## 3. Test site and data

### 3.1. Synthetic data

Synthetic surfaces displaying multi-scale concave and convex morphologies were generated to illustrate and test the proposed method's capability for morphology identification and robustness to DEM noise. Because both profile and tangential curvature were utilized to quantify land surface morphology along two orthogonal directions, synthetic surfaces were constructed using two different configurations. For profile curvature measuring the rate of change of slope gradient along the slope direction, synthetic surfaces were created based on the hyperbolic tangent function. The 1D version of the hyperbolic tangent function is given in Eq. (5) (Brzank et al. 2008).

$$z(x) = s\tanh(f(x+p)) + k \tag{5}$$

Parameter $s$ is a scale factor that determines the height difference between the upper and lower plateau. Parameter $f$ controls the horizontal distance between two curve edges, i.e., the points of maximum curvature. The distance decreases as $f$ increases. Parameter $p$ shifts the function along the $x$-axis, whereas parameter $k$ shifts the function along the $z$-axis. An example of the 1D version of the hyperbolic tangent function is shown in Fig. 2, with $s = 1$, $f = 1$, $p = 0$ and $k = 0$.

The 2D version (see Eq. (6)) of the hyperbolic tangent function used in this study is given by

$$z(x, y) = s \tanh(f(x + p)) + k + ty \ , \tag{6}$$

where the additional parameter $t$ controls the slope of the function in the direction of the $y$-axis. Because profile curvature quantifies the surface morphology in the slope direction, $t$ is assigned to zero in this case so that the slope direction is along the $x$-axis. The shape described by Eq. (6) simulates landslide morphological features such as a scarp with a convex morphology at its upper edge and a concave morphology at its lower edge. The synthetic surface generated using Eq. (6) was sampled on a regular grid with a cell size of 0.2×0.2 to produce synthetic DEM data. Fig. 3A displays the synthetic surface composed of three segments separated by two black dash lines, which are characterized by both concave and convex morphologies of different scales and distinctness. The values of the two parameters controlling the shape of each segment are given in Table 1. A slice of the synthetic data extracted along the $x$-axis is shown in Fig. 3B. The first segment consisted of two step-like curves with the same shape. Compared with the other two segments, segment 1 had the smallest scale factor $s$ and the largest value of parameter $f$, resulting in concave and convex morphologies of the smallest scale at the curve edges. The curve in segment 3 is characterized by concave and convex morphologies that are less distinct than the other two segments.

Table 1 Parameters controlling the shape of each segment of the synthetic surface created on the basis of the hyperbolic tangent function

| Parameter | Segment 1 | Segment 2 | Segment 3 |
|---|---|---|---|
| $s$ | 0.5 | 1 | 0.6 |
| $f$ | 2 | 1 | 0.6 |

The synthetic data shown in Fig. 3A are a regular sample of a smooth surface. To examine the effect of DEM noise, random numbers generated from a normal distribution with a mean value of 0 were added to the original synthetic data. The standard deviation of the normal distribution was specified based on the roughness of the synthetic surface (Berti et al. 2013). First, data detrending was undertaken to remove the general sloping trend of the original synthetic surface by subtracting the elevation of a best fit plane ($z = ax + by + c$, where $a$, $b$ and $c$ are parameters estimated through least squares fitting) from the elevation values of the cells in the synthetic data. The roughness of the synthetic surface was then represented by the root-mean-square (RMS) height (Shepard et al. 2001)

$$\xi = \left[ \frac{1}{n-1} \sum_{i=1}^{n} (z_i - \bar{z})^2 \right]^{1/2} , \tag{7}$$

where $n$ is the number of sample points, $z_i$ is the height of the detrended surface at point $i$, and $\bar{z}$ is the mean height of the detrended surface. The standard deviation of the normal distribution was finally specified as $0.05 \times \xi$. A small multiplier 0.05 was selected so that the noise added to the synthetic data did not conceal the roughness of the synthetic surface. A slice of the noise-adding synthetic data is shown in Figs. 3C and 3D.

For tangential curvature defined in the direction normal to the slope direction, a synthetic surface was created based on the trigonometric sine function as follows

$$z(x, y) = A\sin(f \cdot y + p) + k + tx\,, \tag{8}$$

where $A$ represents the wave amplitude, $f$ is the period of wave oscillation, which determines the distance between two adjacent peaks or troughs, $p$ is the phase shift, $k$ shifts the function along the $z$-axis, and $t$ controls the slope of the function along the $x$-axis. The synthetic surface created using Eq. (8) is shown in Fig. 4A, which was sampled on a regular grid with a cell size of 0.2×0.2. A slice of the synthetic data extracted along the $y$-axis is shown in Fig. 4B. The surface in Fig. 4A is composed of two segments separated by a black dashed line. The values of parameters $A$ and $f$, which describe the shape of the two segments, are given in Table 2, and parameter $t$, which determines the slope gradient of the synthetic surface was assigned a value of one. As shown in Figs. 4A and 4B, both the concave and convex morphologies of segment 1 had smaller scales than those of segment 2. Subsequently, random noise was added to the synthetic data following the method described above, and a slice of the synthetic data with noise is shown in Figs. 4C and 4D.

Table 2 Parameters controlling the shape of each segment of the synthetic surface created based on the sine function

| Parameter | Segment 1 | Segment 2 |
|---|---|---|
| $A$ | 1 | 2 |

| | | |
|---|---|---|
| $f$ | 1 | 0.5 |

### 3.2. Test site covered by airborne LiDAR data

An area located on the west coast of Lantau Island in Hong Kong was selected to test the proposed morphological feature extraction method. Hong Kong is a Special Administrative Region of China and has an area of approximately 1100 km$^2$. It is situated on the South China Sea and has a subtropical monsoonal climate, with a mean annual rainfall of 2800 mm (Parry 2011). Lantau Island is an outlying island located in the southwestern part of Hong Kong. Most of the island is occupied by hills and mountains with steep slopes. Due to the large amounts of rainfall and steep slopes, Lantau Island is susceptible to landslides, most of which are debris slides and flows (Dai and Lee 2002). The selected test site (Fig. 5) covers an area of approximately 0.8 km$^2$, with elevations ranging from 1.5 m to 373.8 m. The mean slope gradient is 28º and the maximum slope gradient is 75º. The rugged land surface within the study area is covered by a variety of vegetation, including grasses, shrubs and woods.

Most of the landslides in the test area are debris slides or flows that usually have a source area empty of failed material, a main scarp which is a steep surface at the upper part of the source area, and a landslide trail downslope of the source where landslide mass transport predominates (Dai and Lee 2002). In addition, most landslides within the test area are probably of translational type with planar failure surfaces, since translational sliding is the predominant failure mode on Lantau Island (Dai and Lee 2002).

The Enhanced Natural Terrain Landslide Inventory (ENTLI) database provided by the Geotechnical Engineering Office of the Hong Kong Civil Engineering and Development Department was made available for this study. ENTLI was created by visually interpreting historical aerial photographs dating from 1924 to 2009 with nominal scales of 1:3000 to 1:40000. It recorded each landslide location using a single point from the landslide crown and the centreline of the landslide trail. According to ENTLI records, a swarm of landslides occurred in 2008 on Lantau Island. The test site was selected owing to a concentration of the most recent landslides. A total of 176 landslides, including 44 in 2008, two between 2006 and 2007, and the rest before 2000, were recorded by ENTLI in the test area. ENTLI also recorded the main scarp widths for all identified landslides. Within the test area, the minimum, maximum and mean main scarp widths were 2, 69 and 12 m, respectively.

An airborne LiDAR survey that covered the entire territory of Hong Kong was conducted between December 2010 and January 2011 (Lai *et al*. 2012). During the survey, the aircraft, which carried an Optech ALTM Gemini LiDAR sensor, flew at altitudes ranging from 1000 m to 1200 m with a nominal 50% overlap between the swaths of adjacent flight lines. The LiDAR data, which contained up to four returns for each pulse, were collected at the maximum point spacing of 0.5 m. The ground verification results indicated that the horizontal and vertical accuracies of the LiDAR data were 0.3 and 0.1 m, respectively. The LiDAR point cloud was classified as ground and non-ground points using the automatic and manual routines in TerraSolid. The results of the automatic routines were checked by trained LiDAR operators and were manually edited when the classification results were incorrect. Using the LiDAR ground points within the test area, a DEM of 1-m resolution was generated for profile and tangential curvature computation.

## 4. Results

### 4.1. Test on synthetic data

The calculations of curvature and local $G_i$* were conducted on the synthetic data shown in Figs. 3 and 4. The local $G_i$* were calculated on each cell using distance thresholds of 0.4, 0.6, 0.8, 1.0, and 1.2, with an interval equalling the cell size.

For the synthetic data created based on the hyperbolic tangent function, both concave and convex morphologies were found along the slope direction, and profile curvature was thus calculated. A slice of curvature values extracted in the direction of $x$-axis are shown in Fig. 6A, in which the three segments are separated by two short black lines. In the graph, there are a total of four peaks and four troughs that correspond to the curve edges with locally maximum curvature values. Due to the abrupt slope changes around the edges, large positive ($>M+1\times\sigma$) or negative ($<M-1\times\sigma$) curvature values were present at the edges of segments 1 and 2. In contrast, segment 3 was characterized by relatively small curvature values due to its gentle slope change. The largest $G_i$* value for all distances was recorded on each cell, and the resultant values along the slice of synthetic data in Fig. 3B are displayed in Fig. 6B, within which $z_{\mathrm{prof}}$ represents the $G_i$* values in Z score standardized form. By comparing Figs. 6A and 6B, we can see that the local $G_i$* graph and profile curvature graph have similar shapes. The locally maximum $G_i$* values in the graph were present around the curve edges

characterized by locally maximum curvature values. By comparing $G_i$* values against a predetermined threshold, in this case 1.96, which is associated with a significance level of 0.05, the significant pattern of clustering of high or low profile curvature values is recognizable around all the curve edges.

After adding noise to the synthetic data, the influences on profile curvature (Fig. 7A) and local $G_i$* (Fig. 7B) values differed. An approximately random profile curvature result was generated from the noisy synthetic data. In comparison with the profile curvature values in Fig. 6A, the result shown in Fig. 7A contained more peaks and troughs, and the curvature values fluctuated irregularly. The curve edges characterized by locally maximum curvature values in the original synthetic data are unrecognizable in Fig. 7A. In contrast with the profile curvature graph, the local $G_i$* graph was less influenced by the noise in the synthetic data. As shown in Fig. 7B, for segments 1 and 2 with more abrupt slope changes, the peaks and troughs corresponding to the curve edges remained recognizable and the local spatial pattern remained significant at a 0.05 significance level. For segment 3, due to its gentle change in slope, the noise had greater influence on its local $G_i$* values than for the other two segments, and no significant spatial pattern is recognizable. These results indicate that the proposed morphological feature extraction method based on local $G_i$* is robust to DEM noise to a certain degree.

The synthetic surface (Fig. 4) created based on the sine function contains two valleys and two ridges. Tangential curvature quantifies the concave or convex morphology in the direction normal to the slope direction. Therefore, as shown in Fig. 8A, the tangential curvature had locally maximum positive values at the ridges and locally maximum negative values at the valleys. Because segment 1 was characterized by concave and convex morphologies of smaller scales, it had relatively abrupt slope changes and hence larger curvature values at its ridge or valley. By comparing the local $G_i$* values (Fig. 8B) and the critical value at a significance level of 0.05, the significant pattern of clustering of high or low tangential curvature values is recognizable at the ridges and valleys.

Similar to the results shown in Fig. 7, the noise added to the synthetic data exerted different effects on tangential curvature (Fig. 9A) and local $G_i$* (Fig. 9B). The tangential curvature values fluctuated irregularly, and the ridges and valleys are unrecognizable from the graph in Fig. 9A. In contrast, the local $G_i$* values around the ridges and valleys remained beyond the critical value at a significance level of 0.05, despite the presence of small fluctuations. This indicates that the significant pattern of clustering of high or low tangential curvature values remained recognizable and the proposed method based on local $G_i$* was capable of identifying the morphology, even under the influence of DEM noise.

### 4.2. Test on airborne LiDAR data

Based on the main scarp width records in ENTLI and observations of recent landslide scars from an aerial photo acquired in 2008, the following distance threshold series was adopted: 2, 3, 4, 5, and 6 m. When extracting morphological features represented by significant local spatial patterns, significance tests were performed at two significance levels: 0.05 and 0.01. All the cells showing significant local patterns in their neighbourhood were extracted for further analysis.

A sample of the results for the profile curvature image is displayed in Fig. 10. The extracted cells are overlain on a 1-m hillshade map generated from LiDAR-derived DEM. Using the aerial photo acquired in 2008, the boundaries of the landslides that occurred in the same year were delineated and are shown in Fig. 10 as solid purple lines. The boundaries of those landslides before 2008 were not delineated because their scars have been partly or totally revegetated. Both ENTLI landslide records and the landslide boundaries delineated from the aerial photo are shown in the figure to facilitate the analysis of the results of the proposed method. For each cell extracted based on the significance tests, the distance thresholds corresponding to the maximum local $G_i$* are indicated in different yellow or blue colours.

As shown in Fig. 10A, the cells were extracted due to a significant local pattern of clustering of high (large positive) profile curvature values found in their neighbourhood, indicating a convex morphology defined along the slope direction. The extracted cells aggregating at the upper borders of the landslide scars therefore reflect the convex morphology of the upper edge of the main scarp. Fig. 10B shows the extracted cells, on which a significant pattern of clustering of low (large negative) profile curvature values is identifiable. The aggregation of the extracted cells downslope of the upper borders of the landslide scars indicates the concave morphology of the lower edge of the main scarp. To further illustrate the morphology of the main scarp, a graph of a profile (profile 1 in Fig. 10A) extracted from a main scarp is shown in Fig. 11A. In fact, the shape of the profile indicates that this landslide, which has a planar failure surface within the source area, is of the translational type (Dai and Lee 2002). According to the graph, a main scarp is a surface with high slope gradients relative to the upslope crown area and the downslope failure surface. Due to an abrupt slope change, large positive and negative profile curvature values cluster at the upper and lower edges of the main scarp, respectively. Therefore, the main scarp is characterized by both an upslope convex morphology and a downslope concave morphology. This pattern can be revealed by identifying the significant pattern of clusters of high or low profile curvature values at both main scarp edges. In the sample area, such a main scarp pattern is identifiable for all recent landslides that occurred in 2008 and one historical landslide that occurred decades ago. The historical landslide (circle in Fig. 10A) has a relatively distinct scar that can be clearly recognized from the hillshade map and hence a significant local pattern of clustering of large profile curvature values at its main scarp edges. In contrast, no significant pattern is identifiable for the remaining historical landslides. Under long-term effects of surface processes, most historical landslide scars have been smoothed, and the local pattern characterizing a main scarp is no longer distinct. In addition to main scarps, there were extracted cells inside landslide scars and in non-sliding areas. Those cells indicate concave or convex morphologies unrelated to main scarp.

The results displayed in Figs. 10A and 10B were obtained at a significance level of 0.05. When more strict significance tests were conducted at a significance level of 0.01, fewer cells were extracted (see Figs. 10C and 10D). The three landslides highlighted by squares in Fig. 10C are characterized by a significant local pattern only at main scarp lower edges at the 0.01 significance level, whereas no significant pattern is seen at their upper edges. The ellipse in Fig. 10C shows a contrary situation. Both situations are probably due to the less distinct edges and subsequent smaller local $G_i$* values for the main scarps in the squares and ellipse. Moreover, in Fig. 10, the different yellow or blue colours indicate the scales at which the local $G_i$* were a maximum, i.e., the maximization of the significance of the local pattern. The variation from light to dark colours at the main scarp edges resulted from the graduated change in the profile curvature values along the slope direction, as shown in Fig. 11A. A large-size aggregation of extracted cells, mainly shown in dark colours, signifies a large-scale concave or convex morphology, whereas an isolated cell in a light colour indicates a small-scale one.

It should be noted that in the areas located downslope of the main scarps, only a small number of cells were extracted, indicating a lack of large-scale significant patterns of clustering of large profile curvature values within the source areas. According to the definition of local $G_i$*, the lack of large-scale significant local patterns is probably due to a planar surface with small profile curvature values approximating zero or a rugged one with varying curvature values summing to zero. By analyzing the main scarp profile shown in Fig. 11A, the former is considered more possible, also taking into account the observations of Dai and Lee (2002) that most landslides on Lantau Island, including the test area, are of the translational type with planar failure surfaces.

Fig. 12 displays a sample of the extraction result from the tangential curvature image. As shown in Fig. 12A, the significant pattern of clustering of high tangential curvature values is identifiable mainly in the areas between landslide scars, indicating a ridge-like convex morphology. When a higher significance level of 0.01 was adopted, fewer cells were extracted (Fig. 12C). In both Figs. 12A and 12C, the large-scale significant pattern of clustering of high tangential curvature values predominates. In Fig. 12B, the cells extracted through identifying a significant pattern of clustering of low tangential curvature values are shown to have congregated inside all of the recent landslide scars and along historical landslide trails. The trails and source areas covered by the extracted cells were characterized by a concave morphology defined in the direction normal to the slope direction. A cross-section (profile 2 in Fig. 10A) extracted from a landslide source area is displayed in Fig. 11B to illustrate that concave morphology. Although fewer cells were extracted when applying a higher significance level of 0.01 (Fig. 12D), large-scale significant patterns predominate at both significance levels. Unlike other landslides, the scar of the one highlighted by a circle in Fig. 12B was occupied by both clusters of high and low tangential curvature values, indicating a rugged surface within its scar.

By comparing Figs. 10 and 12, we find that the significance level had more effect on the extraction result of the profile curvature image than on that of the tangential curvature image. At a lower significance level of 0.05, the significant pattern of clustering of high or low profile curvature values was recognized on both main scarp edges for all of the recent landslides and one historical landslide. However, at a higher significance level of 0.01, many fewer landslides were characterized by such a significant pattern on both main scarp edges. In contrast, for the tangential curvature image, almost all of the landslide source areas and trails within the sample area were characterized by a concave morphology at both significance levels.

### 4.3. Extraction of landslide morphological features using curvature thresholds

For comparison with the proposed method, we attempted to extract landslide morphological features represented by concave or convex morphologies based solely on the curvature values on individual cells. The LiDAR data in the same test area on Lantau Island, Hong Kong were utilized. First, thresholds were defined for the profile and the tangential curvature image. Because the profile and tangential curvature values in the test area approximately followed normal distributions, thresholds in the form of $M \pm n \times \sigma$ were applied to the curvature images, where $n$, M and σ represent a multiplier, the mean and the standard deviation of all the curvature values, respectively. Those cells with curvature values beyond the thresholds were extracted to indicate the concave or convex morphological features on the land surface. Results for the profile and the tangential curvature image in a sample area are shown in Figs. 13 and 14 respectively.

When small thresholds ($M_{Prof} \pm 1\times\sigma$) were applied to the profile curvature image (Figs. 13A and 13B), a number of cells around the upper borders of the landslide scars were extracted, indicating the concave or convex morphologies of the main scarp edges. However, under the effect of DEM noise, the extracted cells along the main scarp edges tended to be disconnected, and one main scarp could correspond to several isolated cells and small-size clusters. As a result, the convex upper edges and concave lower edges of the main scarps could not be clearly recognized. In addition, a large number of isolated cells and clusters of sizes smaller than 3 cells were scattered over the sample area, resulting in a ‘salt-and-pepper’ appearance. Most of those isolated cells and small-size cell clusters were potentially unrelated to actual morphological features but resulted from DEM noise. When applying larger thresholds of $M_{Prof} \pm 2\times\sigma$ (Figs. 13C and 13D), the number of isolated cells and small-size clusters decreased substantially, but simultaneously a much fewer number of cells along the main scarp edges were extracted. Contrarily, by applying the proposed method to the profile curvature image, the cells extracted by identifying significant local patterns congregated at the main scarp edges (Fig. 10), and the number of isolated cells and small-size clusters within and outside the landslide scars was small.

For the tangential curvature image, the cells extracted at small thresholds of $M_{Tang} \pm 1\times\sigma$ were scattered both inside and outside the landslide scars (Figs. 14A and 14B). A number of extracted cells with low tangential curvature values congregated within landslide scars, indicating a concave morphology created by material removal. However, due to a large number of isolated cells and small-size clusters of high or low curvature values, the concave morphologies of the source areas and trails could not be clearly revealed. The application of larger thresholds ($M_{Tang} \pm 2\times\sigma$) reduced the number of extracted cells inside and outside landslide scars simultaneously (Figs. 14C and 14D). Despite the fewer number of isolated cells and small-size clusters, the concave source areas and trails were almost unrecognizable due to the fragmentation of the extracted cell clusters. In contrast, using the proposed method, the cells extracted by identifying a significant pattern of clustering of low tangential curvature values congregated within landslide scars, forming relatively large-size clusters (Fig. 12), and the concave source areas and trails could be clearly recognized from the results.

## 5. Discussion

### 5.1. Capability of being robust to DEM noise

The high density of the LiDAR point cloud allowed small-scale morphological features on the land surface to be captured. However, noise in LiDAR-derived DEMs may depress the distinctiveness of morphological features and thus lead to great difficulty in extracting morphological features, especially small scale features (Passalacqua et al. 2010a; Li et al. 2011). That situation was illustrated in this study using synthetic grid data. For a smooth curving surface, both concave and convex morphologies were characterized by large curvature values and were clearly recognizable from the local $G_i^*$ graphs through comparison with the critical value at a specific significance level. When small random noise was added to the synthetic data, the curvature values began to fluctuate irregularly. In that situation, identifying concave or convex morphologies based solely on curvature values is difficult and false morphological features will be extracted.

In the literature, methods have been proposed to reduce the effects of DEM noise. One solution is to apply noise reduction methods. Li et al. (2011) smoothed and coarsened a LiDAR-derived DEM to reduce artefactual depressions in the DEM. Noise reduction was also implemented in Lashermes et al. (2007) and Passalacqua et al. (2010b) based on wavelets and nonlinear filtering, respectively. The risk of noise reduction is that small-scale features may be smoothed out simultaneously or become indistinct in lower resolution DEMs. Another solution is to extract morphological features by identifying spatial patterns rather than considering the values on individual

DEM cells. The spatial patterns of morphological features usually remain recognizable under the influence of DEM noise, whereas the values of individual DEM cells are altered by DEM noise. Most studies have characterized the spatial patterns of surface roughness or topographical variability (e.g., Glenn et al. 2006; Trevisani et al. 2009; Whelley et al. 2014). The method proposed in this study focuses on landslide morphological features represented by homogeneous local patterns.

By identifying local patterns of clustering of similar curvature values, the proposed method based on local $G_i$* has the capability of being robust to DEM noise. In comparison to the curvature graphs, the local $G_i$* graphs were less influenced by the noise added to the synthetic data and both concave and convex morphologies were recognizable, with the exception of those for the curve edges with gentle slope changes in segment 3 (see Fig. 3). The comparison between the proposed method and the method based on curvature thresholds using airborne LiDAR data further proved the proposed method's robustness to DEM noise. The results of the method based on curvature thresholds had a 'salt and pepper' appearance and the morphology of landslide main scarps, source areas and trails could not be clearly recognized. Using the proposed method, more cells related to landslide morphological features were extracted through the identification of significant spatial patterns of clustering of high or low curvature values. Those cells did not necessarily have large curvature values. They were extracted because the majority of the curvature values in their neighborhood were large and had the same sign, resulting in a large total sum of curvature values and thus a large local $G_i$* value. Because the focus is on the sum of curvature values, the effect of DEM noise on individual values can be greatly reduced. This is also the reason why the number of the isolated cells extracted by the proposed method was small.

### 5.2. Extraction of multi-scale morphological features

In the proposed method, the issue of extracting multi-scale landslide morphological features was dealt with by applying a series of distance thresholds and utilizing the largest local $G_i$* value to indicate the distinctiveness of the morphological features. This is similar to the moving window method, which analyzes indicators of land surface morphology using multiple window sizes. The difference is that, for the extraction of landslide morphological features, moving window methods usually need to determine the most appropriate window size for the entire area by comparing the results of different window sizes (e.g., Tarolli et al. 2012; Berti et al. 2013). However, window size selection is a difficult process because a single window size is commonly inadequate for large areas characterized by complex terrain (Schmidt & Andrew 2005). The proposed method utilizes multiple neighbourhood sizes to calculate local $G_i$* and adopts the largest $G_i$* value to indicate a local pattern of maximum significance, which is equivalent to selecting a window size most appropriate for a local area. In this way, the determination of a specific threshold relevant to morphological feature scale is avoided, and we only need to define the range of distance thresholds based on landslide size information (widths and lengths) in the study area.

The necessity of adopting the multi-scale method was proved by the test results of the airborne LiDAR data. Figs. 10 and 12 display the extracted cells in different colours based on the distance threshold corresponding to the maximum significance. The light-coloured cells indicate that the local patterns have maximum significances at relatively small scales. If a single large distance threshold rather than a series of thresholds had been applied, those cells might not have been extracted due to insignificant local patterns, and the corresponding landslide morphological features could not be identified. The situation is the same for the dark-coloured cells, which indicate the local patterns having maximum significances at relatively large scales.

### 5.3. Potential application in landslide detection

The method proposed in this study was tested in an area on Lantau Island, Hong Kong, within which small-size debris slides and flows predominate. Main scarps composed of a convex upper edge and a concave lower edge were indicated by the cells extracted from the profile curvature image and aggregated around the upper borders of landslide scars. Both concave and convex morphologies were defined along the slope direction. In addition, for most recent landslides, no large-scale significant local pattern was recognized in the source areas. This phenomenon supports the observation of Dai and Lee (2002) that the majority of the landslides on Lantau Island are of translational type with planar failure surfaces. However, planar failure surface features could not be extracted by the proposed method and other local statistics that can distinguish between planar and rugged morphologies may be considered in further studies. Along landslide trails, both significant patterns of clustering of high and low profile curvature values were recognizable but the latter prevailed. This is probably because landslide mass transport predominated along trails, although material deposition also occurred (Dai and Lee 2002). Mass transport resulted in concavities, whereas deposition brought about convexities. The extraction results of the tangential curvature image indicate that most landslides in the test area were characterized by concave source areas and trails. The concave morphology is defined in the cross-sectional direction, i.e., the direction perpendicular to the slope direction. However, a number of recent landslides with relatively wide main scarps were shown to have undulating rupture surfaces within the source areas, as both significant local patterns of clustering of high and low tangential curvature values were present.

Using the proposed method, the cells extracted from the profile or tangential curvature image congregated along main scarp edges or within source areas and trails, forming clusters of different sizes. Those cell clusters potentially represent landslide main scarps, source areas and trails. Therefore, by extracting corresponding cell clusters, landslide morphological features are identified, which could be used to help detect and map landslides. To evaluate that potential, all ENTLI-recorded landslides in the test area were classified as those having identifiable morphological features, including main scarps, source areas and trails, and those without. A main scarp was regarded to be identifiable if cells with high local $G_i$* values calculated from the profile curvature image congregated along the main scarp's upper edge, and cells with low local $G_i$* values congregated along its lower edge. A source area or a trail was regarded to be identifiable if cells with low local $G_i$* values calculated from the tangential curvature image congregated within it. The planar morphology (defined along the slope direction) of the source area was not considered since it was expressed by small local $G_i$* values, i.e., insignificant local patterns. The cells related to a planar failure surface of source area and those related to rough terrain could not be directly distinguished. The Hong Kong landslide inventory ENTLI records each landslide using a point from the crown and the centreline of the mass trail. Within a specified distance (3 m in this study) from each ENTLI crown point, cell clusters related to main scarp edges were searched. Because source area and trail are not differentiated in ENTLI, along each ENTLI trail line, cell clusters with low local $G_i$* values calculated from the tangential curvature image were searched, which might represent a source area, trail or both. The search results are displayed in Table 3. Almost all recent landslides (< 5 years) had both identifiable main scarps and trails, indicating that those landslides can be detected using the proposed method. In contrast, only 45 out of 130 historical landslides (⩾ 10 years) have both identifiable main scarps and trails. This is because under long-term effects of surficial processes, the morphological features of those historical landslides were no more distinct.

Although its potential application in landslide detection has been proved, the proposed method can only be used as a first step due to the simultaneous extraction of a large number of cell clusters unrelated to landslides (see Figs. 10 and 12). More landslide-unrelated cell clusters were extracted in woodland than in grassland (the sample area shown in Figs. 10 and 12 is grassland), probably due to the rough terrain or incorrect classification of the LiDAR point cloud in woodland, which resulted in artefactual morphological features. A higher significance level (e.g., 0.01) could not effectively decrease the number of landslide-unrelated cell clusters while preserving those representing landslide morphological features. To detect and map landslides, a filtering strategy should be applied to remove landslide-unrelated clusters based on supplementary information provided by expert knowledge or other data sources. For instance, the relative positions between cell clusters related to main scarps and trails should be considered in the filtering strategy. Cell clusters related to main scarp lower edges should be located downslope of those related to upper edges. The former should be located upslope of cell clusters related to trails. Passive optical images such as aerial photos or satellite imagery are important sources of data that are used to provide spectral information for landslide detection (Joyce et al. 2014). The development of the filtering procedures should be considered in further studies. Furthermore, most recent landslides within the test area were located in grassland, and thus the capability of LiDAR for extracting morphological features under forest canopies was not discussed. Using LiDAR data of adequate point density and an appropriate point cloud classification method, landslide detection in forested areas based on the proposed method is also possible, and needs to be evaluated in further studies.

Table 3 ENTLI-recorded landslides having identifiable morphological features. The landslides were categorized based on their ages up to the date of the acquisition of the LiDAR data.

| Age of landslide | 0~5 years | 5~10 years | 10~20 years | >20 years |
|---|---|---|---|---|
| Number of landslides with identifiable features | 45 | 0 | 1 | 44 |
| Total number of landslides | 46 | 0 | 4 | 126 |

## 6. Conclusions

In this study, a multi-scale method based on local $G_i$* statistic was proposed for extracting landslide morphological features characterized by homogeneous local patterns of clustering of similar morphometric values. Both profile and tangential curvature were utilized to quantify land surface morphology. To represent landslide morphological features, cells with significant local patterns of clustering of similar curvature values in their neighbourhood were extracted from curvature images through significance tests. To test the proposed method, we used both synthetic surfaces and airborne LiDAR data acquired over an area of Lantau Island, Hong Kong. The synthetic surfaces simulated natural terrain characterized by concave and convex morphologies of different scales and distinctness along two perpendicular directions (slope direction and cross-sectional direction). Random noise was added to the synthetic grid data to evaluate the robustness of the proposed method to DEM noise.

The test results of the synthetic data show that even under the effect of DEM noise, the convex or concave morphologies of the simulated terrain features, represented by large positive or negative local $G_i$* values, were recognizable from the local $G_i$* graphs. In contrast, the noise added to the synthetic data brought about a great influence on curvature values, and neither convex nor concave morphologies could be recognized from the curvature graphs.

The test conducted on the airborne LiDAR data shows that the proposed method is capable of extracting the morphological features of shallow debris slides and flows. The cells extracted from the profile curvature image indicated main scarps with convex upper edges and concave lower edges. Moreover, the planar failure surfaces of the translational landslides were also indicated by the results. The cells extracted from the tangential curvature image indicated the concave source areas and landslide trails, except for those with large main scarp widths. For comparison, cells were also extracted from the profile and the tangential curvature image based on curvature thresholds to indicate landslide morphological features. Due to the influence of DEM noise, a large number of isolated cells and small-size cell clusters were extracted, and the landslide morphological features represented by cells of large curvature values were indistinct.

Finally, the potential of applying the proposed method in landslide detection was evaluated. Using a Hong Kong landslide inventory to verify the extraction result, it was found that 98% of recent landslides (<5 years) had identifiable main scarps and trails, whereas approximately 35% of historical landslides (>10 years) had identifiable morphological features. Those landslides could be automatically detected based on their identifiable morphological features. However, due to the simultaneous extraction of a large number of cell clusters unrelated to landslides, especially in woodland, a cell cluster filtering strategy should be applied based on supplementary information from expert knowledge or other data sources.

## Acknowledgements

Acknowledgement is made to the Head of the Geotechnical Engineering Office and the Director of the Civil Engineering and Development, the Government of the Hong Kong Special Administrative Region (SAR), for permission to use the LiDAR data. The authors also gratefully acknowledge the support of the research fund of Zhejiang A&F University (2015FR023) and Education of Zhejiang Province (Y201636125).

## References

Ardizzone, F., Cardinali, M., Galli, M., Guzzetti, F., Reichenbach, P., 2007. Identification and mapping of recent rainfall-induced landslides using elevation data collected by airborne LiDAR. Natural Hazards and Earth System Sciences 7(6), 637-650.

Berti, M., Corsini, A., Daehne, A., 2013. Comparative analysis of surface roughness algorithms for the identification of active landslides. Geomorphology 182, 1–18.

Booth, A.M., Roering, J.J., Perron, J.T., 2009. Automated landslide mapping using spectral analysis and high-resolution topographic data: Puget Sound lowlands, Washington, and Portland Hills, Oregon. Geomorphology 109, 132–147.

Boots, B., 2002. Local measures of spatial association. Ecoscience 9(2), 168-176.

Brzank, A., Heipke, C., Goepfert, J., Soergel, U., 2008. Aspects of generating precise digital terrain models in the Wadden Sea from lidar–water classification and structure line extraction. ISPRS Journal of Photogrammetry & Remote Sensing 63, 510-528.

Chu, C.M., Tsai, B.W., Chang, K.T., 2009. Integrating Decision Tree and Spatial Cluster Analysis for Landslide Susceptibility Zonation. World Academy of Science, Engineering and Technology 35, 479-483.

Dai, F.C., Lee, C.F., 2002. Landslide characteristics and slope instability modeling using

GIS, Lantau Island, Hong Kong. Geomorphology 42, 213–228.

Derksen, C., Wulder, M., LeDrew, E., Goodison, B., 1998. Associations between spatially autocorrelated patterns of SSM/I-derived prairie snow cover and atmospheric circulation. Hydrological Processes 12, 2307–2316.

Evans, I.S., 1972. General geomorphometry, derivatives of altitude, and descriptive statistics. In: Chorley, R.J. (Ed.), Spatial Analysis in Geomorphology. Methuen, London, pp. 17–90.

Getis, A., Aldstadt, J., 2004. Constructing the spatial weights matrix using a local statistic. Geographical Analysis 36(2), 90–104.

Getis, A., Ord, J.K., 1992. The Analysis of Spatial Association by Use of Distance Statistics. Geographical Analysis 24, 189-206.

Glenn, N.F., Streutker, D.R., Chadwick, D.J., Thackray, G.D., Dorsch, S.J., 2006. Analysis of LiDAR-derived topographic information for characterizing and differentiating landslide morphology and activity. Geomorphology 73, 131–148.

Griffith, P., Getis, A., Griffin, E., 1996. Regional patterns of affirmative action compliance costs. The Annals of Regional Science 30, 321-340.

Grohmann, C.H., Smith, M.J., Riccomini, C., 2011. Multiscale Analysis of Topographic Surface Roughness in the Midland Valley, Scotland. IEEE Transactions on Geoscience and Remote Sensing 49(4), 1200–1213.

Guzzetti, F., Mondini, A.C., Cardinali, M., Fiorucci, F., Santangelo, M., Chang, K.T., 2012. Landslide inventory maps: New tools for an old problem. Earth-Science Reviews 112, 42–66.

Jaboyedoff, M., Oppikofer, T., Abellán, A., Derron, M.H., Loye, A., & Metzger, R., Pedrazzini, A., 2012. Use of lidar in landslide investigations: a review. Natural Hazards 61(1), 5-28.

Joyce, K.E., Samsonov, S.V., Levick, S.R., Engelbrecht, J., Belliss, S., 2014. Mapping and monitoring geological hazards using optical, LiDAR, and synthetic aperture RADAR image data. Natural Hazards 73, 137–163.

Kalbermatten, M., Van De Ville, D., Turberg, P., Tuia, D., Joost, S., 2012. Multiscale analysis of geomorphological and geological features in high resolution digital elevation models using the wavelet transform. Geomorphology 138, 352-363.

Kasai, M., Ikeda, M., Asahina, T., Fujisawa, K., 2009. LiDAR-derived DEM evaluation of deep-seated landslides in a steep and rocky region of Japan. Geomorphology 113, 57–69.

Krcho, J., 1991. Georelief as a subsystem of landscape and the influence of morphometric parameters of georelief on spatial differentiation of landscape-ecological processes. Ecology (CSFR) 10, 115–157.

Lai, A.C.S., So, A.C.T., Ng, S.K.C., Jonas, D., 2012. The territory-wide airborne light detection and ranging survey for the Hong Kong Special Administrative Region. The 33rd Asian Conference on Remote Sensing, Pattaya, Thailand, November 2012.

Lanorte, A., Danese, M., Lasaponara, R., Murgante, B., 2013. Multiscale mapping of burn area and severity using multisensor satellite data and spatial autocorrelation analysis. International Journal of Applied Earth Observation & Geoinformation

20(2), 42-51.

Lashermes, B., Foufoula-Georgiou, E., Dietrich, W.E., 2007. Channel network extraction from high resolution topography using wavelets. Geophys. Res. Lett. 34, L23S04.

Li, S., MacMillan, R.A., Lobb, D.A., McConkey, B.G., Moulin, A., Fraser, W.R., 2011. Lidar DEM error analyses and topographic depression identification in a hummocky landscape in the prairie region of Canada. Geomorphology 129, 263-275.

Li, X., Cheng, X., Chen, W., Chen, G., Liu, S., 2015. Identification of Forested Landslides Using LiDar Data, Object-based Image Analysis, and Machine Learning Algorithms. Remote Sensing 7(8), 9705-9726.

Mackey, B.H., Roering, J.J., 2011. Sediment yield, spatial characteristics, and the long-term evolution of active earthflows determined from airborne LiDAR and historical aerial photographs, Eel River, California. Geological Society of America Bulletin 123(7-8), 1560-1576.

Mckean, J., Roering, J., 2004. Objective landslide detection and surface morphology mapping using high-resolution airborne laser altimetry. Geomorphology 57(3–4), 331-351.

Nelson, A., Oberthür, T., Cook, S., 2007. Multi-scale correlations between topography and vegetation in a hillside catchment of Honduras. International Journal of Geographical Information Science 21(2), 145-174.

Ord, J.K., Getis, A., 1995. Local Spatial Autocorrelation Statistics. Geographical

Analysis 27, 286–306.

Parry, S., 2011. The Application of Geomorphological Mapping in the Assessment of Landslide Hazard in Hong Kong. In: Smith, M.J., Paron, P., Griffiths, J.S. (Eds.), Geomorphological mapping: methods and applications. Elsevier, pp. 413–441.

Passalacqua, P., Tarolli, P. Foufoula-Georgiou, E., 2010a. Testing space-scale methodologies for automatic geomorphic feature extraction from lidar in a complex mountainous landscape. Water Resources Research 46, W11535.

Passalacqua, P., Do Trung, T., Foufoula-Georgiou, E., Sapiro, G., Dietrich, W.E., 2010b. A geometric framework for channel network extraction from LiDAR: Nonlinear diffusion and geodesic paths. J. Geophys. Res. 115, F01002.

Petschko, H., Bell, R., Glade, T., 2016. Effectiveness of visually analyzing LiDAR DTM derivatives for earth and debris slide inventory mapping for statistical susceptibility modeling. Landslides 13, 1-16.

Schmidt, J., Evans, I.S., Brinkmann, J., 2003. Comparison of polynomial models for land surface curvature calculation. International Journal of Geographical Information Science 17(8), 797–814.

Schmidt, J., & Andrew, R., 2005. Multi-scale landform characterization. Area 37(3), 341–350.

Shepard, M.K., Campbell, B.A., Bulmer, M.H., Farr, T.G., Gaddis, L.R., & Plaut, J.J., 2001. The roughness of natural terrain: a planetary and remote sensing perspective. Journal of Geophysical Research 106(E12), 32777–32795.

Soeters, R., van Westen, C.J., 1996. Slope instability recognition, analysis and zonation.

In: Turner, A.K., Schuster, R.L. (Eds.), Landslides, Investigation and Mitigation, Special Report 247. Transportation Research Board, Washington D.C. pp. 129-177.

Tarolli, P., Sofia, G., Fontana, G.D., 2012. Geomorphic features extraction from high-resolution topography: landslide crowns and bank erosion. Natural Hazards 61(1), 65-83.

Trevisani, S., Cavalli, M., Marchi, L., 2009. Variogram maps from LiDAR data as fingerprints of surface morphology on scree slopes. Natural Hazards and Earth System Sciences 9, 129–133.

Turner, M.G., O'Neill, R.V., Gardner, R.H., Milne, B.T., 1989. Effects of changing spatial scale on the analysis of landscape pattern. Landsc. Ecol. 3, 153 – 162.

Van Den Eeckhaut, M., Kerle, N., Poesen, J., Hervas, J., 2012. Object-oriented identification of forested landslides with derivatives of single pulse LiDAR data. Geomorphology 173-174(9), 30-42.

Whelley, P.L., Glaze, L.S., Calder, E.S., Harding, D.J., 2014. LiDAR-Derived Surface Roughness Texture Mapping: Application to Mount St. Helens Pumice Plain Deposit Analysis. IEEE Transactions on Geoscience and Remote Sensing 52(1), 426-438.

Wulder, M., Boots, B., 1998. Local spatial autocorrelation characteristics of remotely sensed imagery assessed with the Getis statistic. International journal of remote sensing 19(11), 2223–2231.

Zevenbergen, L.W., Thorne, C., 1987. Quantitative analysis of land surface topography. Earth Surface Processes and Landforms 12, 47–56.

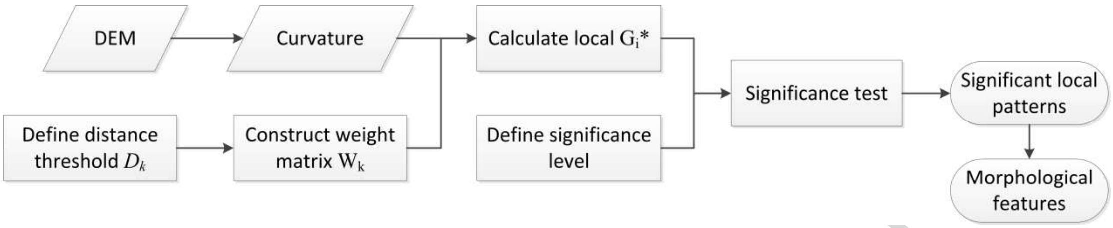

Fig. 1. Flowchart of the method for extracting morphological features

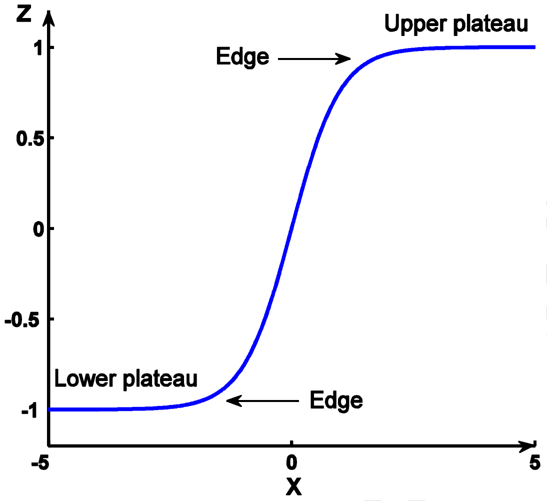

Fig. 2. Hyperbolic tangent function

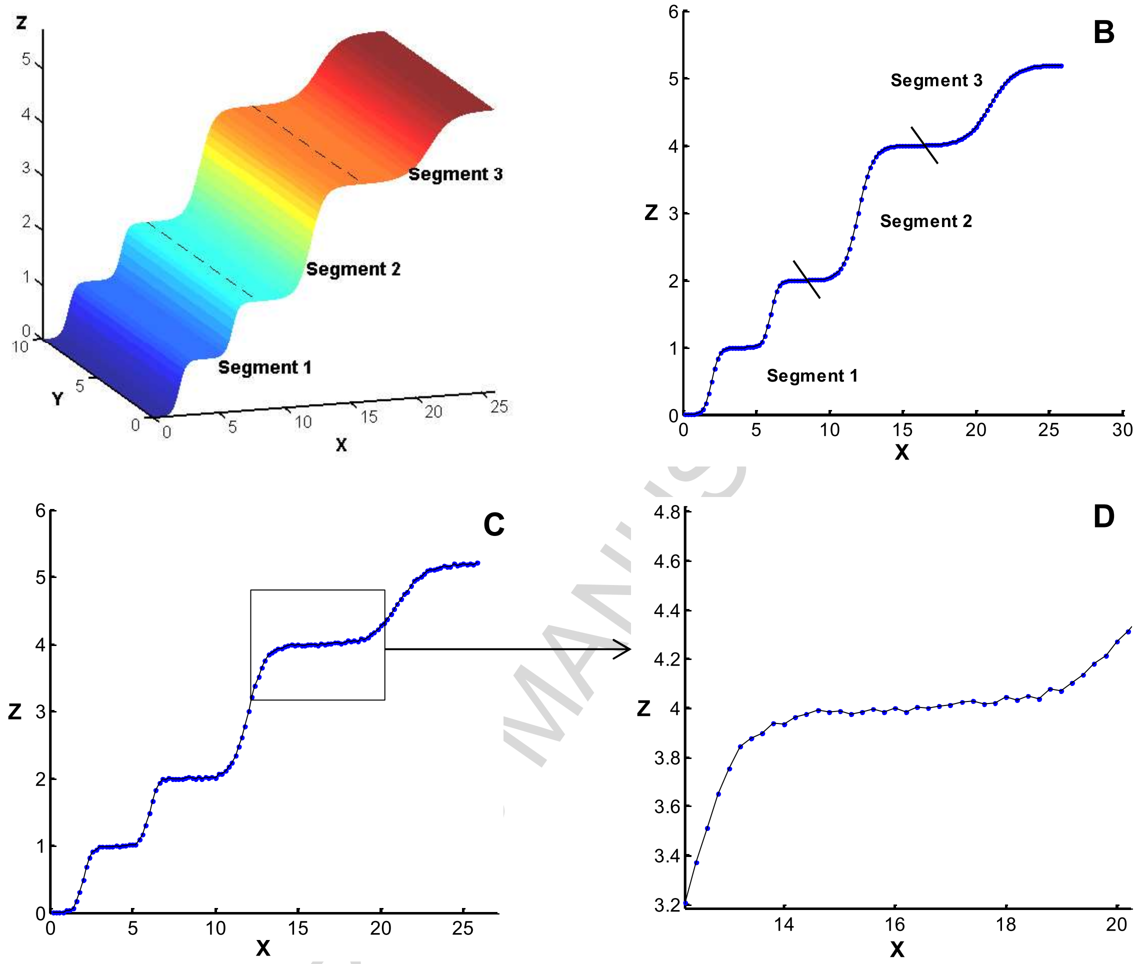

Fig. 3. Synthetic data created based on the hyperbolic tangent function. (A) Synthetic surface composed of three segments. (B) Slice of synthetic data along the *x*-axis. (C) Slice of the synthetic data with noise along the *x*-axis. (D) Enlargement of a part of the curve in (C).

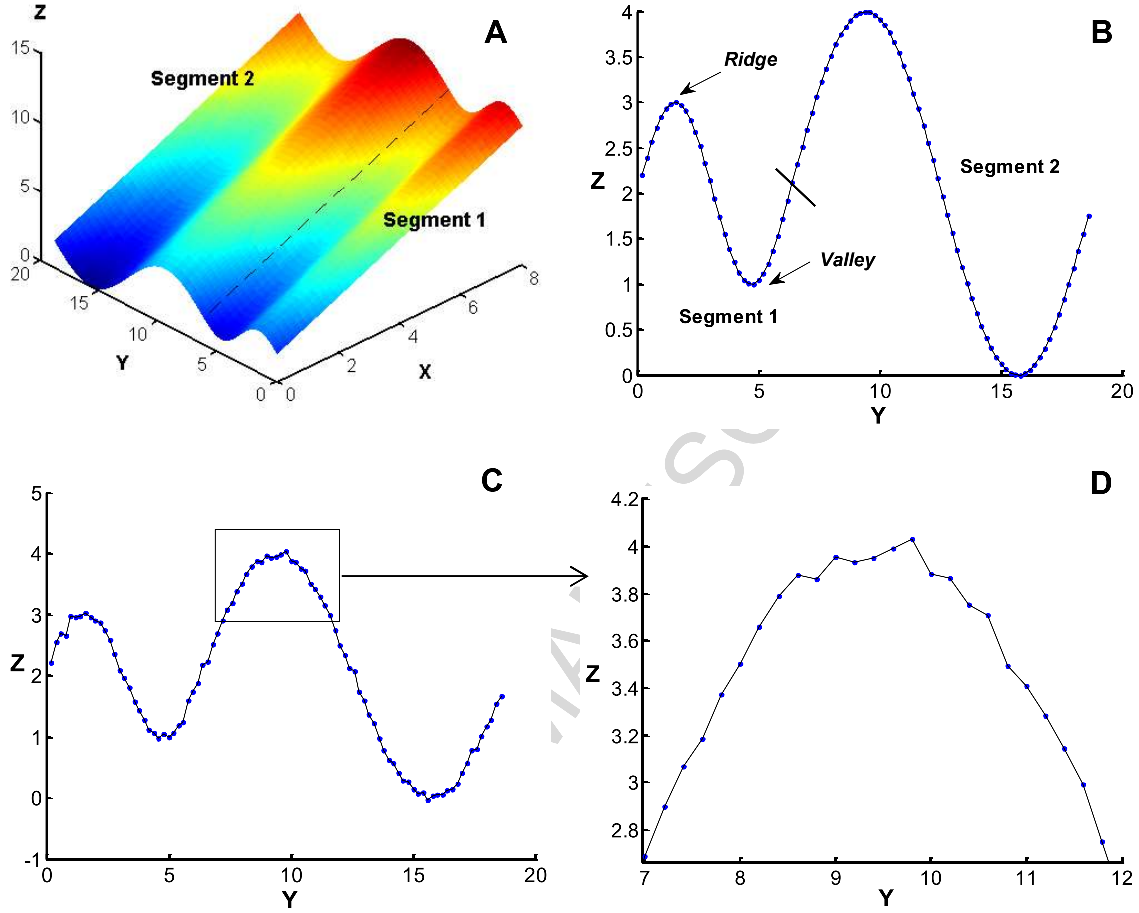

Fig. 4. Synthetic data created based on the sine function. (A) Synthetic surface composed of three segments. (B) Slice of synthetic data along the *y*-axis. (C) Slice of the synthetic data with noise along the *y*-axis. (D) Enlargement of a part of the curve in (C).

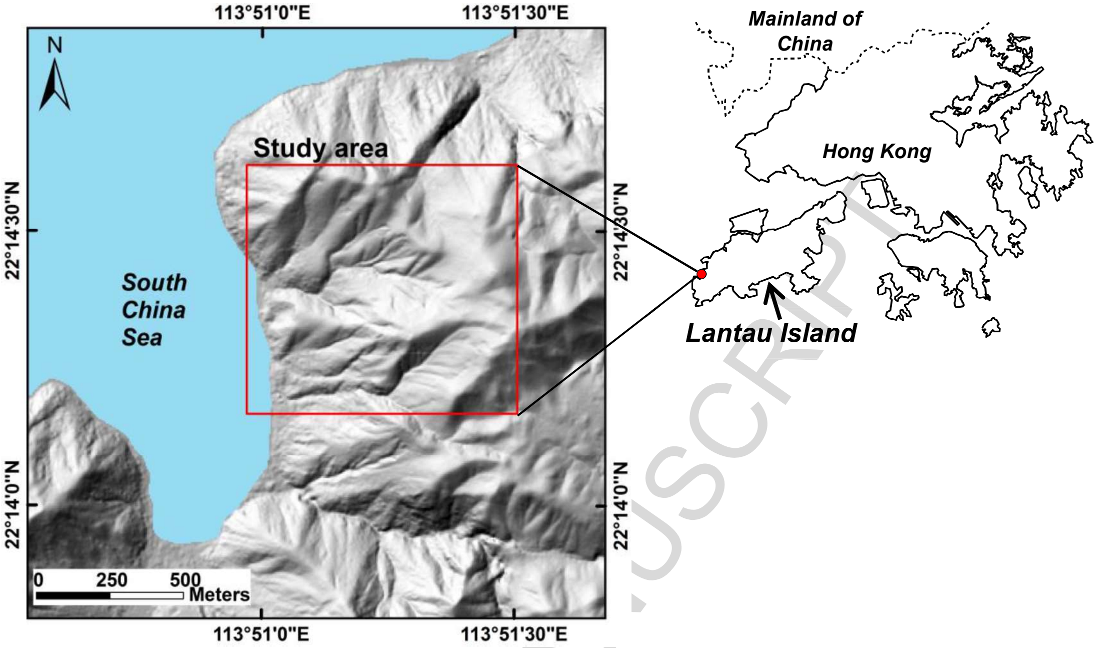

Fig. 5. Test area located on the west coast of Lantau Island, Hong Kong.

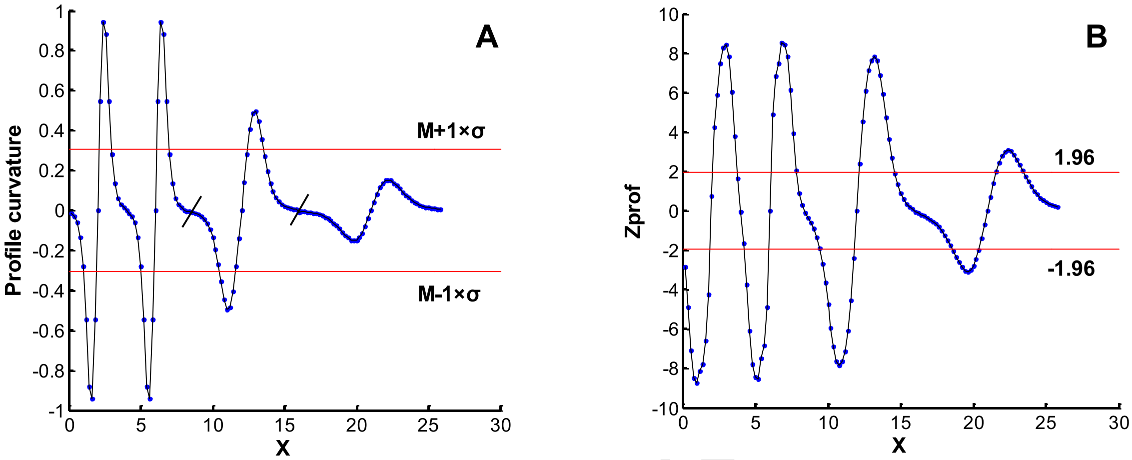

Fig. 6. Profile curvature and local $G_i^*$ ($Z_{\text{prof}}$) values along the slice of the synthetic data shown in Fig. 3B. M and σ represent the mean and the standard deviation of all profile curvature values, respectively.

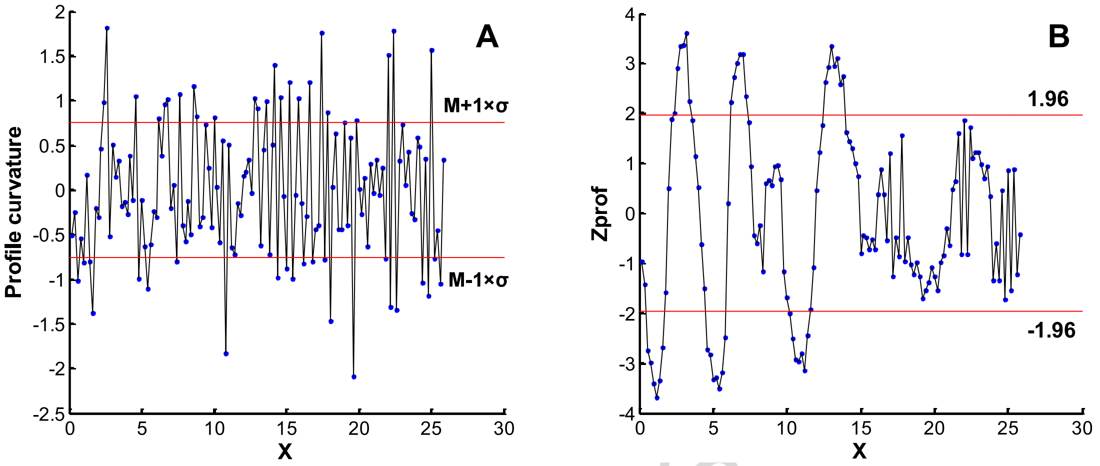

Fig. 7. Profile curvature and local $G_i^*$ ($Z_{\mathrm{prof}}$) values along the slice of the synthetic data with noise shown in Fig. 3C. M and σ represent the mean and the standard deviation of all profile curvature values, respectively.

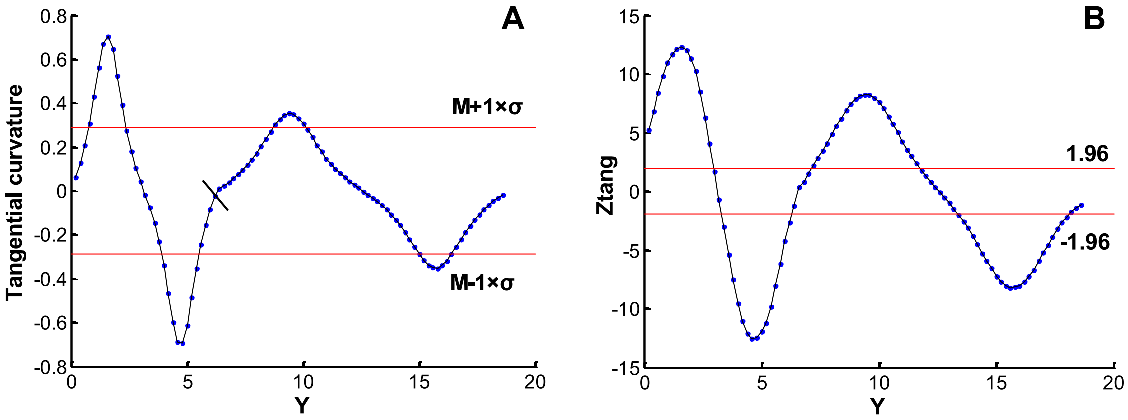

Fig. 8. Tangential curvature and local $G_i$* ($Z_{tang}$) values along the slice of the synthetic data shown in Fig. 4B. M and σ represent the mean and the standard deviation of all tangential curvature values, respectively.

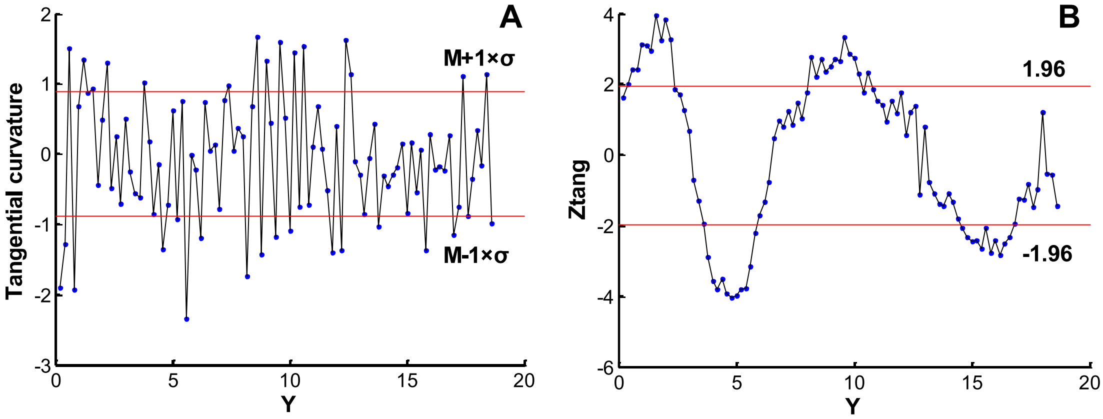

Fig. 9. Tangential curvature and local $G_i^*$ ($Z_{\text{tang}}$) values along the slice of the synthetic data with noise shown in Fig. 4C. M and σ represent the mean and the standard deviation of all tangential curvature values, respectively.

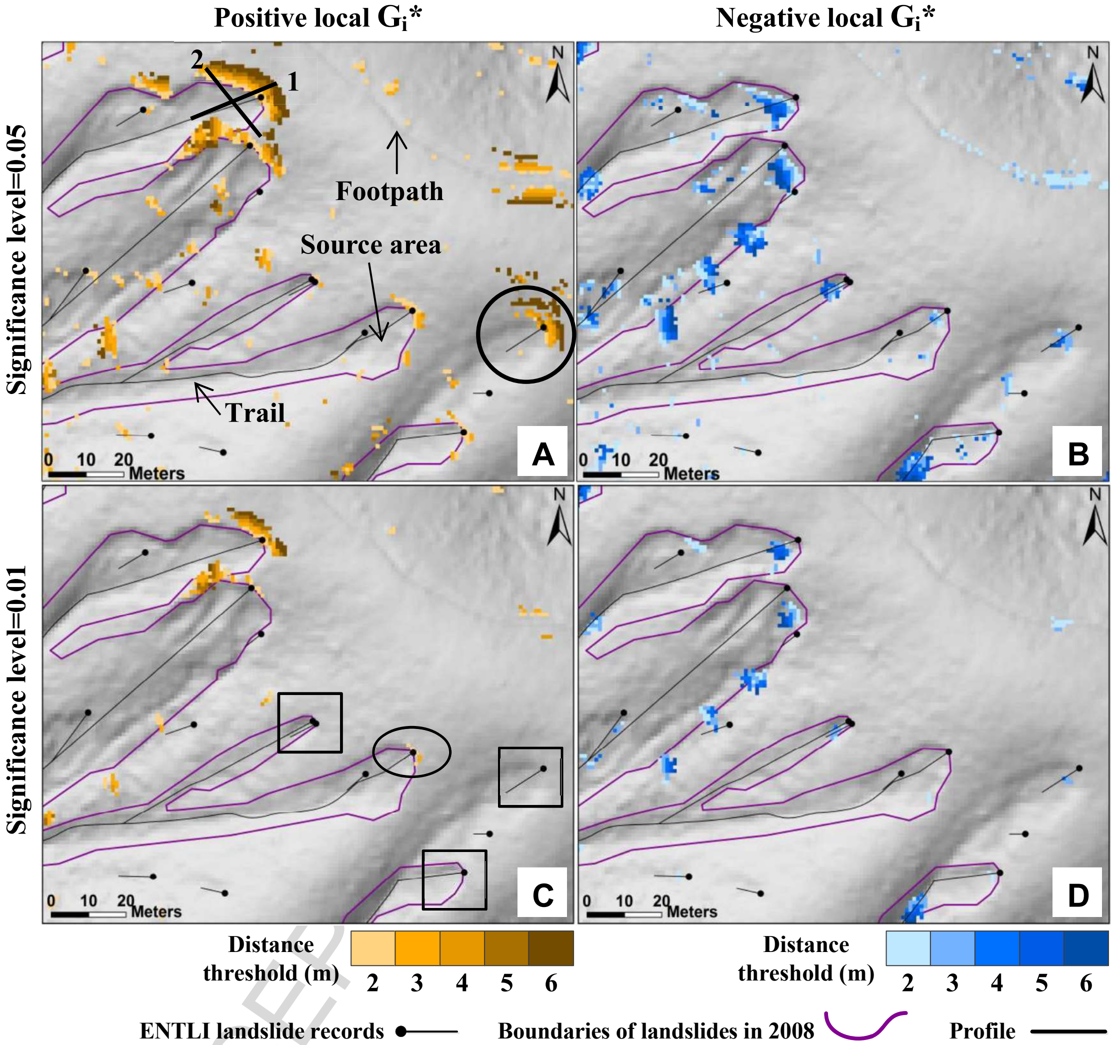

Fig. 10. Cells extracted from the profile curvature image through identifying the significant local patterns of clustering of high or low profile curvature values at different significance levels. The circle indicates a historical landslide characterized by the significant local patterns of clustering of large profile curvature values at both main scarp edges. The squares and ellipse highlight the landslides characterized by significant local patterns only at lower or upper main scarp edges at the higher significance level of 0.01.

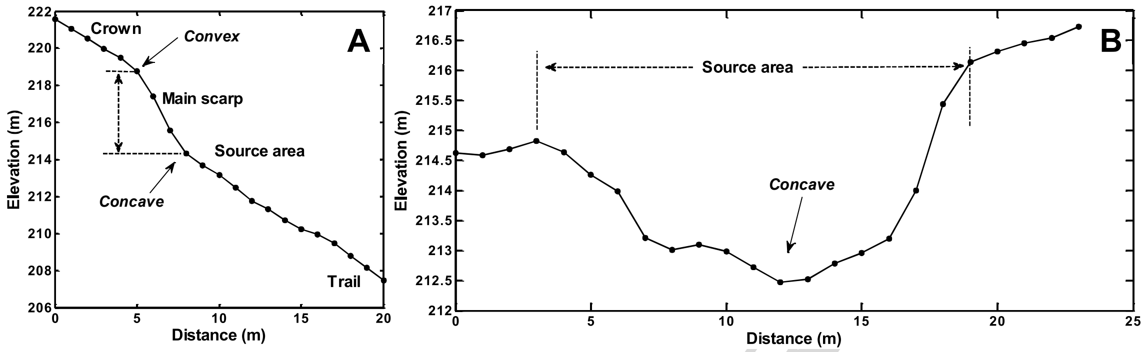

Fig. 11. Profile graphs generated from the LiDAR-derived DEM. (A) Graph of profile 1 (Fig. 10A) extracted from a main scarp along the slope direction. (B) Graph of profile 2 (Fig. 10A) traversing a source area.

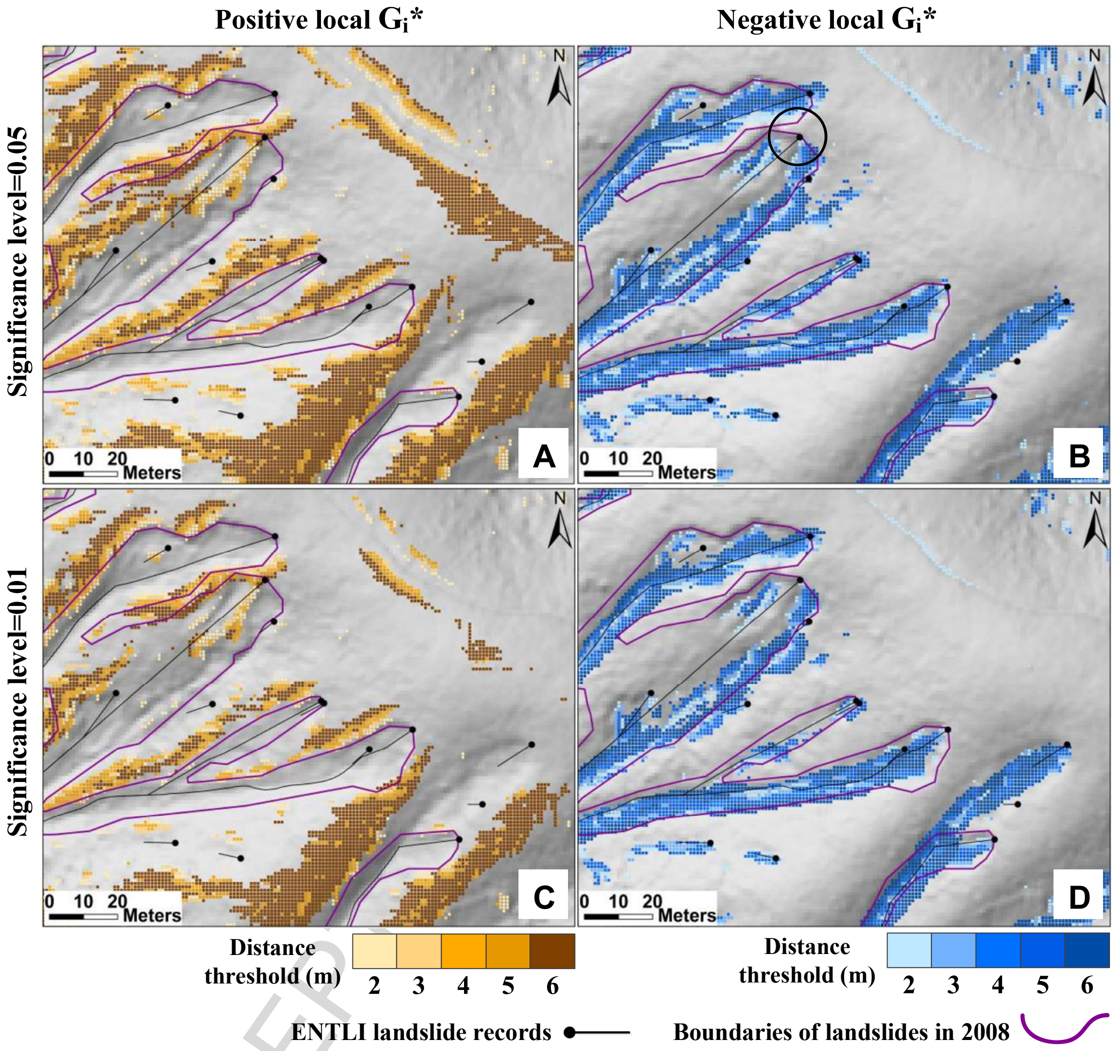

Fig. 12. Cells extracted from the tangential curvature image through identifying the significant local patterns of clustering of high or low tangential curvature values at different significance levels. The circle highlights a landslide characterized by both significant patterns of clustering of high and low tangential curvature values in its scar.

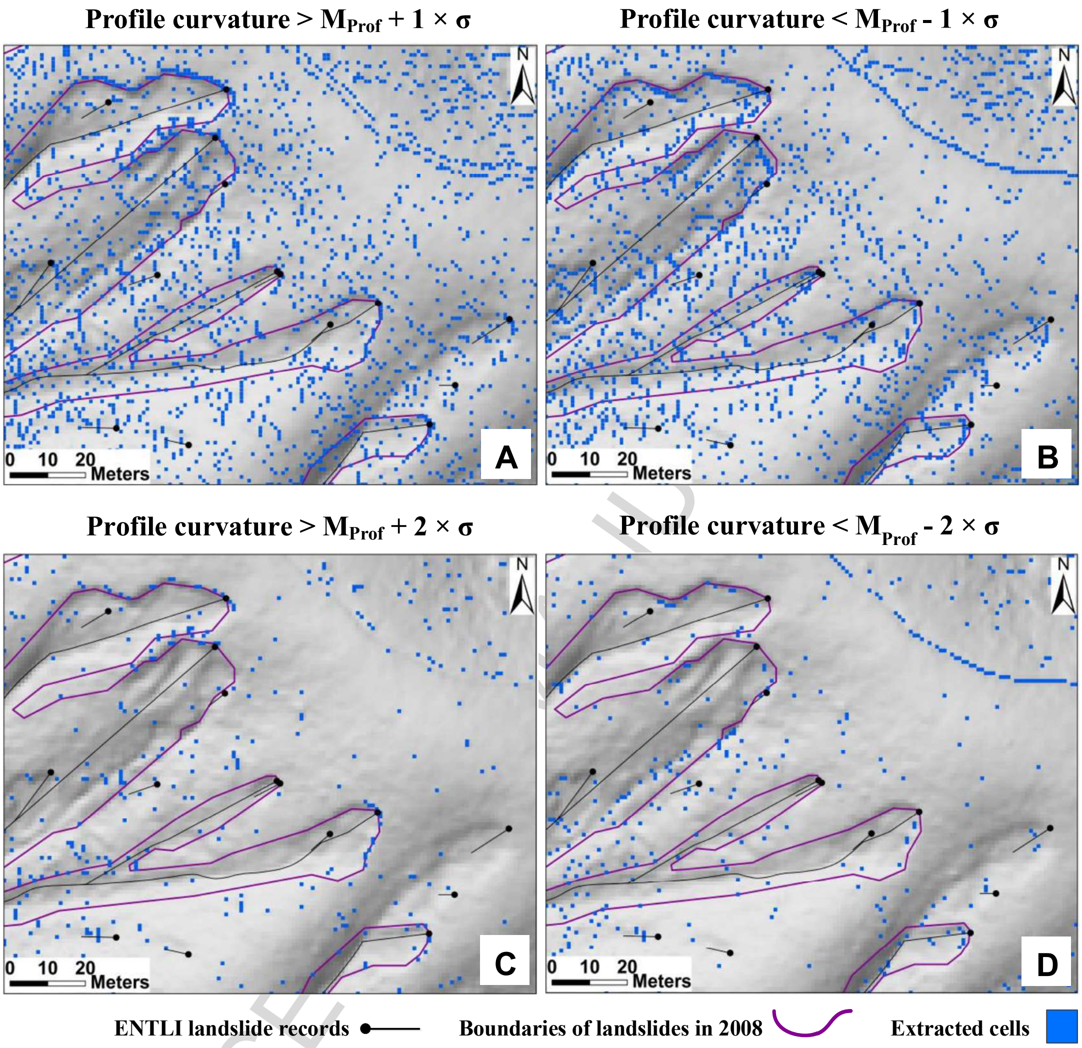

Fig. 13. Cells extracted based on profile curvature thresholds. $M_{Prof}$ and σ are the mean and the standard deviation of all profile curvature values, respectively.

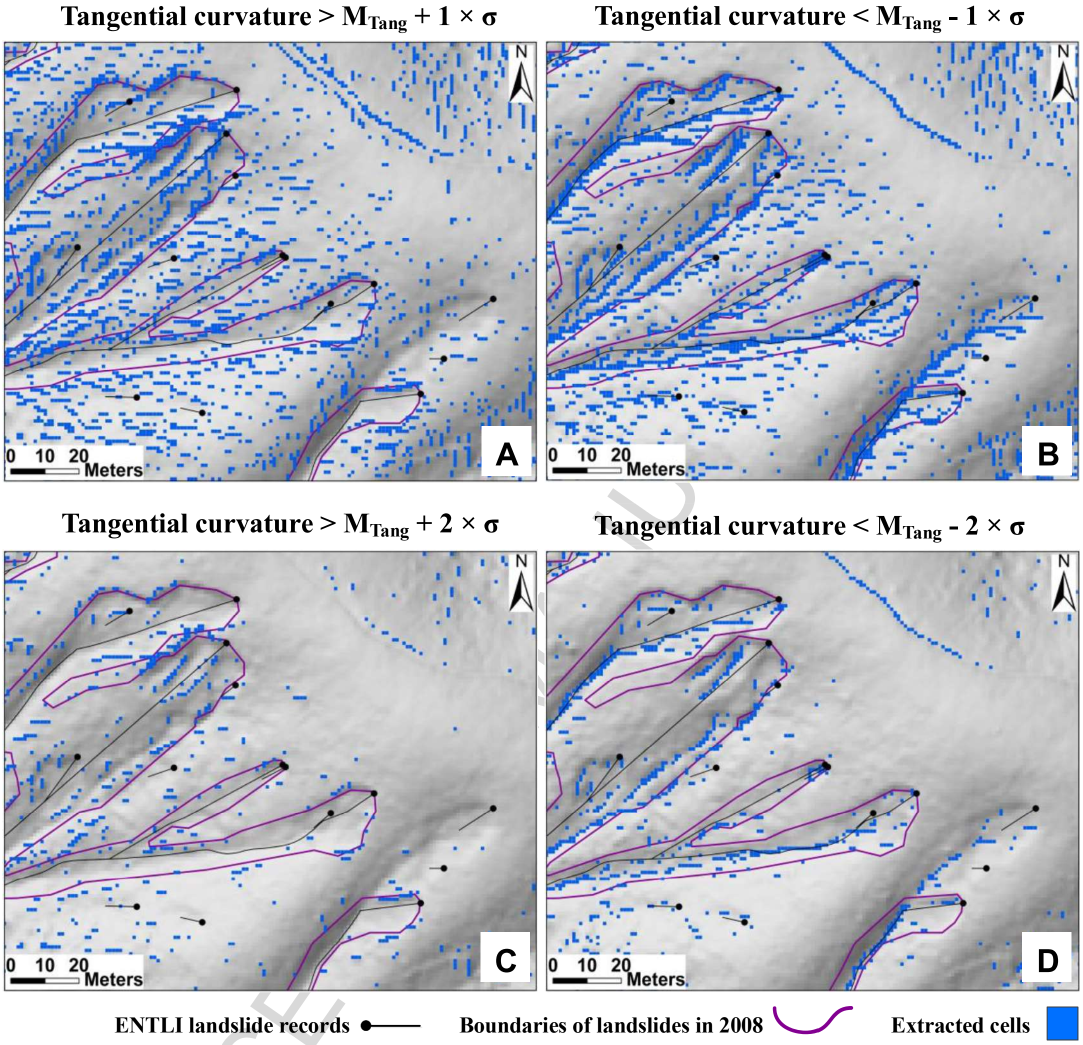

Fig. 14. Cells extracted based on tangential curvature thresholds. $M_{Tang}$ and σ are the mean and standard deviation of all tangential curvature values, respectively.

**Highlights**

- A multi-scale landslide morphological feature extraction method is proposed.
- The method based on local $G_i$* is robust to the noise in high resolution DEM.
- The method can be utilized to extract morphological features represented by a homogeneous spatial pattern.
- The morphological features of shallow debris slides and flows can be extracted using the proposed method.